Modeling and Control of Swing Oscillation of Underactuated Indoor Miniature Autonomous Blimps

Qiuyang Tao[a], Tun Jian Tan[b], Jaeseok Cha[c], Ye Yuan[d], Fumin Zhang[a,*]

[a] *School of Electrical and Computer Engineering, Georgia Institute of Technology*
Atlanta, GA 30332, USA

[b] *Department of Electronic and Computer Engineering, The Hong Kong University of Science and Technology*
Hong Kong SAR, China

[c] *School of Mechanical Engineering, Georgia Institute of Technology*
Atlanta, GA 30313, USA

[d] *School of Automation, Huazhong University of Science and Technology*
Wuhan, Hubei 430074, China

This paper presents the dynamic modeling and flight control system design that reduce the swing oscillation of an underactuated indoor miniature autonomous blimp (MAB). Indoor MAB features outstanding safety and flight endurance, but swing oscillation is often observed due to their underactuated design and unique aerodynamic shape. A grey box model is established to describe the dynamics of the swing motion, and the model parameters are identified from physical measurements and experimental data. A flight control system is designed to reduce the swing oscillation with features including low latency and center-of-mass position estimation. The modeling and control methods are applied to the Georgia-Tech miniature autonomous blimp (GT-MAB) during hovering flight. The experimental results show that the proposed methods can effectively reduce the swing oscillation of GT-MAB.

Keywords: Miniature autonomous blimp; dynamic modeling; flight control.

1. Introduction

Indoor aerial robots are gaining increasing attention owing to their promising applications including surveillance, building exploration, and search and rescue [1–3]. Human-robot interaction with indoor airborne robots is a growing research trend in recent years [4, 5]. However, most existing indoor aerial platforms, such as quadcopters, have fast-spinning propellers which may cause safety concerns in human-occupied indoor environments [6]. Besides, these platforms usually have limited flight endurance [7], which restricts their applications. Lighter than air robots (LTARs) keep themselves aloft without the need for consistent motor action. Hence, LTARs are the most power efficient unmanned aerial systems [7], and their endurance can be several orders of magnitude greater than that of heavier-than-air vehicles [8]. The extended flight endurance makes LTARs well-suited to many applications that require sustained airborne presence [8]. However, the size of LTARs is usually at the scale of a couple meters [9], such that it can obtain sufficient amount of buoyancy [7, 10]. As a consequence, most LTARs are designed for outdoor applications instead of indoor purposes.
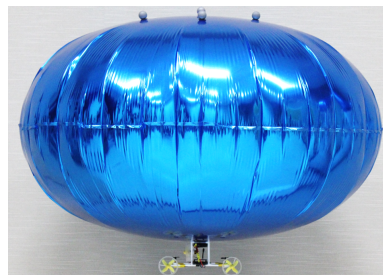

Fig. 1.   GT-MAB assembly with localization markers and gondola installed at the top and the bottom of the envelop.

We develop the Georgia Tech Miniature Autonomous Blimp (GT-MAB), a small-sized LTAR specifically designed for indoor applications [11]. Owing to the light-weight mechatronics design, the diameter of GT-MAB is

---

*Email Address: fumin@gatech.edu

2   *Q.Tao et al.*

only around 0.7 meters while still guarantees payload capacity for devices including IMU and wireless camera [12]. The miniature size of GT-MAB ensures its mobility in indoor spaces. As shown in Fig. 1, GT-MAB is cushioned with a helium-filled envelop, making the robot safe to fly indoors, causing no threat to human and the surroundings even with collisions. With the lifting force provided by buoyancy, GT-MAB has flight endurance for more than 2 hours [13, 14]. Our previous works have investigated the dynamics model and the controller design for the translational and steering motion of GT-MAB, and developed autopilot systems that can navigate the blimp in 3D space [13, 14]. The existing modeling and control approaches successfully demonstrated their capabilities on GT-MAB, and have been adopted in many applications including environmental sampling [13] and human-robot interaction [6, 14, 15]. However, lateral and longitudinal oscillation is often observed due to the underactuated design and the unique aerodynamic shape of GT-MAB. This undesirable oscillation has impacts on certain applications of GT-MAB. The onboard sensors usually have directionality, and oscillation could cause inaccurate readings. Moreover, the quality of the video stream from the onboard camera is affected by the oscillatory movement. Mechanical gimbals can be installed on aerial robots to stabilize the sensors [16], but such a device may exceed the payload capacity of indoor miniature blimps. Besides, the oscillation consumes extra energy and might cause people to feel less comfortable interacting with the robot. Therefore, it is crucial to study the dynamic model of the swing oscillation, and design controllers to reduce this undesirable motion.

Dynamic modeling of large outdoor airships has long been studied [17]. However, due to the unique design and indoor application of GT-MAB, existing methods for outdoor airships do not apply. In contrast to conventional outdoor airships, which usually have cigar-shaped envelop and tail fins, GT-MAB features a unique tailless "saucer shaped" envelop, to obtain adequate buoyancy, omnidirectional mobility, and outstanding safety in indoor spaces. As a trade-off, existing analytical methods for modeling the conventional cigar-shaped airships, i.e. [18], can hardly be applied to GT-MAB. Moreover, as shown in Fig. 1, there is folding on envelop of GT-MAB. The non-smooth surface makes it hard to accurately construct model and perform CFD (computational fluid dynamics) simulations such as [19]. Besides, hovering and slow-flying are the most common operating scenarios for indoor blimps, while outdoor airships are usually designed for cruising. As a consequence, wind tunnel tests, i.e. [20, 21], are not applicable due to the low speed nature of GT-MAB. In summary, the non-conventional shape, non-smooth envelop, and slow-flying nature of GT-MAB are the major difficulties in modeling the swing motion of GT-MAB.

Due to the limitations including light-weight mechatronics, miniature indoor blimps are not widely available until recently. Only a few projects address the modeling of the conventional cigar-shaped indoor blimps with sizes slightly larger than the saucer-shaped GT-MAB. The existing approaches for modeling the dynamics of indoor blimps can be categorized into two groups, analytical and data-driven. The analytical methods investigate the aerodynamics from the specific shape of the blimp [22].The work [23] presented the dynamics of a cigar-shaped indoor blimp, and simplified the model to separate the translational and steering motion. The model is then further reduced to only considering the horizontal and steering motion for the convenience of studying the control strategy under wind disturbance. However, identification of the parameters, such as the viscous coefficient, was not discussed. The work [24] derived the 6-DOF mathematical model of a cigar-shaped indoor blimp. The pitch and roll angles are assumed to be small, and the model is simplified by removing the roll and pitch dynamics. Authors of [22] modeled the 6-DOF dynamics of an indoor blimp, and developed a simulator based on the model. Parameters of the dynamics model were analyzed given the geometry of the envelop. Unfortunately, all these works [22–24] focus on modeling indoor blimps with cigar-shaped envelop. Since the analytical methods may only be valid for a specific class of envelop shapes [19], existing analytical methods for modeling the traditional cigar-shaped blimps cannot be easily applied to saucer-shaped blimps such as GT-MAB. Data-driven approaches discover the dynamics from data measurements [25]. The work [25] simplified the dynamical equation of an indoor blimp along its vertical axis, and then identified the model parameters from the step response of the vertical motion. The parameters of upward and downward motion are identified separately due to the asymmetric dynamics of the vertical motion. Unfortunately, only vertical motion is considered in this work. Our previous work [14] simplified the dynamics model of GT-MAB into decoupled translational and steering motion. The parameters of each decoupled movement are identified separately. However, the roll and pitch motions were not considered in this work. To the best of our knowledge, our recent work [26] is the only literature on modeling the swing oscillation of saucer-shaped indoor blimps among the existing efforts on developing this type of robot such as [27, 28]. However, controller design on reducing the swing oscillation was not presented in [26].

All onboard electronics of GT-MAB, including the thrusters, are installed on one single 3D printed gondola mounted underneath the envelop. This configuration reduces weight, ensures alignment between thrusters, and enhances the durability of the blimp. However, this underactuated thruster configuration also causes undesired pitching or rolling torque once the motors are on. This disturbance shows a more significant impact on the roll and pitch motion of GT-MAB when more powerful thrusters are installed for better maneuverability and flyability against airflow. Besides, most MABs require external localization systems to fly inside the GPS-denied indoor environment. These systems usually incorporate multiple ceiling-mounted infrared cameras to track the retroreflective markers installed on the robots. The localization markers are usually installed at the top of the envelop for best visibility to the cameras. Measurement from the localization

systems is the pose of the markers. The marker position has constant offset above the CM of GT-MAB and is used to represent the position of the blimp when there is negligible roll or pitch angle. However, the tracker position becomes fluctuated when GT-MAB is swinging, which further aggregates the swing oscillation. Therefore, the CM position of GT-MAB needs to be estimated from the identified swing dynamics model, and incorporated in controller design. Moreover, the external localization system requires a ground station computer to interface with the cameras and to compute the pose of GT-MAB. Other computationally intensive tasks, such as object detection, are also implemented on the ground station computer to save payload and energy. Therefore, wireless communication is required to exchange data between the ground station and onboard electronics of GT-MAB. However, as reported in work [25], control system latency of indoor blimp with external localization device and off-board computing is around 0.2-0.4 seconds. The latency is acceptable to control the relatively slow translational and steering motion of GT-MAB, but cannot satisfy the needs for regulating the fast swing oscillation. As a summary, the main difficulties in reducing the swing motion of GT-MAB are its unique underactuated design, fluctuated position measurement, and latency in the control system.

Flight controllers for existing indoor miniature blimps can be categorized into two groups based on whether a dynamic model is required. Without the dynamics model, the work [29] compared PID and fuzzy logic algorithms for altitude control, and presented a fuzzy logic controller for collision avoidance. Authors of the work [30] presented a biologically based flight controller with visual information from two camera inputs. PID controllers are designed in [10, 31, 32] for motion control and landing. Cooperative control of multiple neural networks is reported in [33] for the robustness with mechanical failures. The work [34] presented a behavior-based navigation system for an indoor blimp. The other portion of the existing literature on controller design incorporates the dynamics model of the blimp. The work [23] studied the control strategy under wind disturbance, and verified the proposed controller design by simulation. Authors of [24] presented both modeling and controller design of a solar-powered indoor blimp. The experimental results showed that the blimp can successfully track a straight path in 3D space. The work [25] designed a predictor-based controller to compensate for the system latency. Experimental results showed the controller can keep the blimp at the desired altitude. However, only the altitude-related modeling and control is considered in [25]. The work [22] designed neuromorphic controllers, and trained the neural network using a simulator with identified dynamics model. The trained controller is then transferred on the physical blimp, and resulted in very similar behavior with the simulated one. Our previous work [14] designed controllers for the translational and steering motion of GT-MAB, and designed a waypoint following controller by combining a set of motion primitives. However, to the best of our knowledge, there is no existing controller design

addressing the swing oscillation of saucer-shaped MABs. In this paper, we extend our previous efforts on modeling the swing motion of GT-MAB by designing a flight control system that reduces this undesired oscillation. The system addresses the difficulties on reducing the swing motion of GT-MAB including the underactuated design, fluctuated position measurement, and latency in the control loop. Feedback controllers are designed based on the identified swing dynamics to regulate the roll and pitch motion of GT-MAB. The CM position of GT-MAB is estimated from the identified swing dynamics and the pose of the blimp. The CM position is then incorporated in the controller design to replace the tracker position for reduced fluctuation. The latency of the control system is improved through better mechatronics design and software implementation. Experiments are conducted to verify the effectiveness of the proposed control system. The experimental results show that the swing oscillation of GT-MAB can be effectively reduced. The swing oscillation is a common problem among indoor miniature blimps. Due to the small size and payload constraints, the bottom-heavy underactuated design is widely adopted by many indoor MABs such as [27, 28]. As a result, the undesired swing oscillation is also inevitable for most indoor MABs besides GT-MAB. Therefore, the proposed methods could be applied to other indoor MABs.

This paper is organized as follows: in Section II, the motion model of GT-MAB is established to describe the swing oscillation. In Section III, the parameters of the swing dynamics are identified, linearized, and validated for controller design. In Section IV, a flight control system is designed to reduce the swing oscillation. In Section V, we draw the conclusion and discuss future work.

2. Motion Model for GT-MAB

In this section, we establish the dynamic model of the miniature indoor blimp, GT-MAB, driven by the gondola-mounted thrusters located underneath the symmetric saucer-shaped envelop.

2.1. *Coordinate Frames*

Fig. 2 shows the definition of the inertial frame, body frame, and the coordinates of the motion capture system. The inertial frame is denoted as O_I-$X_I Y_I Z_I$ with axis Z_I pointing downward. The body frame O_B-$X_B Y_B Z_B$ is established at the buoyancy center of GT-MAB, thus the center-of-volume (CV) of the envelop. We use an optical localization system (OptiTrack) to track the pose of the reflective markers on GT-MAB at millimeter level accuracy. The coordinate system of the motion tracking system is defined as O_L-$X_L Y_L Z_L$ with Y-up convention. For convenience, we let O_L coincide with O_I, and $O_L X_L$ parallel to $O_I X_I$. The localization markers are installed at the top of the envelop for best visibility to the motion tracking system. The pose of the markers in the localization system is denoted as

O_M-$X_MY_MZ_M$. Given the fact that O_M-$X_MY_MZ_M$ is usually calibrated to align with O_B-$X_LY_LZ_L$ when GT-MAB is leveled, we can assume that the plane X_MZ_M is parallel to X_BY_B, and O_MX_M is parallel to O_BX_B.
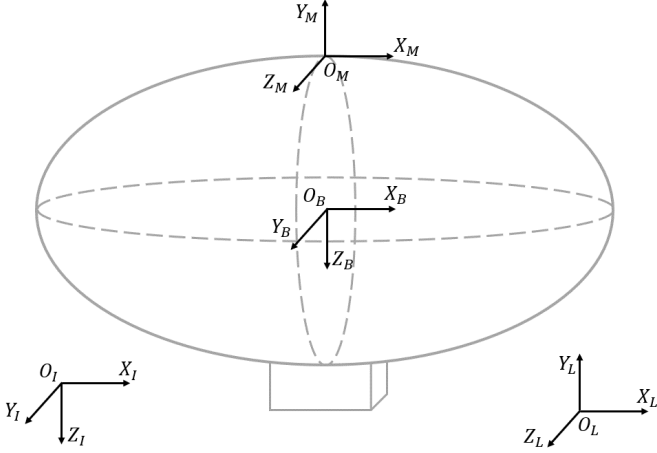

Fig. 2.   Illustration of the coordinate frames.

Let $\boldsymbol{\eta_1} = [x, y, z]^\top$ and $\boldsymbol{\eta_2} = [\phi, \theta, \psi]^\top$ represent position and orientation of GT-MAB in inertial frame. The pose of GT-MAB is denoted as $\boldsymbol{\eta} = [\boldsymbol{\eta_1}, \boldsymbol{\eta_2}]^\top$. Linear and angular velocity of GT-MAB in the body frame is described by $\boldsymbol{v} = [\boldsymbol{V}, \boldsymbol{\Omega}]^\top$, where $\boldsymbol{V} = [u, v, w]^\top$ and $\boldsymbol{\Omega} = [p, q, r]^\top$. According to the work [8], relationship between the velocities in different coordinate frames are given by:

$$\begin{bmatrix} \dot{\boldsymbol{\eta_1}} \\ \dot{\boldsymbol{\eta_2}} \end{bmatrix} = \begin{bmatrix} \boldsymbol{R}(\boldsymbol{\eta_2}) & 0_{3\times3} \\ 0_{3\times3} & \boldsymbol{J}(\boldsymbol{\eta_2}) \end{bmatrix} \begin{bmatrix} \boldsymbol{V} \\ \boldsymbol{\Omega} \end{bmatrix}, \quad (1)$$

where $\boldsymbol{R}(\boldsymbol{\eta_2})$ is the rotation matrix. Using the simplified notation $c\cdot = \cos(\cdot)$ and $s\cdot = \sin(\cdot)$, $\boldsymbol{R}(\boldsymbol{\eta_2})$ has the form of:

$$\boldsymbol{R}(\boldsymbol{\eta_2}) = \begin{bmatrix} c\psi c\theta & -s\psi c\phi + c\psi s\theta s\phi & s\psi s\phi + c\psi s\theta c\phi \\ s\psi c\theta & c\psi c\phi + s\psi s\theta s\phi & -c\psi s\phi + s\psi s\theta c\phi \\ -s\theta & c\theta s\phi & c\theta c\phi \end{bmatrix}. \quad (2)$$

The term $\boldsymbol{J}(\boldsymbol{\eta_2})$ in Equation 1 can be represented as:

$$\boldsymbol{J}(\boldsymbol{\eta_2}) = \begin{bmatrix} 1 & 0 & -s\theta \\ 0 & c\phi & s\phi c\theta \\ 0 & -s\phi & c\phi c\theta \end{bmatrix}^{-1} = \begin{bmatrix} 1 & s\phi \tan\theta & c\phi \tan\theta \\ 0 & c\phi & -s\phi \\ 0 & s\phi/c\theta & c\phi/c\theta \end{bmatrix}. \quad (3)$$

2.2.   Dynamic Model of GT-MAB

From our previous work [14, 26], the generic 6-DOF dynamic model of GT-MAB is given as:

$$m(\dot{\boldsymbol{V}} + \boldsymbol{\Omega} \times \boldsymbol{V}) = \boldsymbol{F} + \boldsymbol{f}$$
$$\boldsymbol{I}\dot{\boldsymbol{\Omega}} + \boldsymbol{\Omega} \times (\boldsymbol{I}\boldsymbol{\Omega}) = \boldsymbol{M} + \boldsymbol{\tau}, \quad (4)$$

where m is the total mass of the blimp, including the mass of the helium gas inside the envelop, and the added mass.

The terms $\boldsymbol{f} = [f_x, f_y, f_z]^\top$ and $\boldsymbol{\tau} = [\tau_x, \tau_y, \tau_z]^\top$ are linear forces and moments generated by the thrusters. Let $\boldsymbol{F} = [F_x, F_y, F_z]^\top$ and $\boldsymbol{M} = [M_x, M_y, M_z]^\top$ represent the sum of forces and moments due to gravity, buoyancy, and other aerodynamic forces acting on the blimp. The terms $\boldsymbol{f}$, $\boldsymbol{F}$, $\boldsymbol{\tau}$, and $\boldsymbol{M}$ are all defined in the body-fixed frame. The symbol $\boldsymbol{I}$ represents the inertia matrix of GT-MAB about CM, which is the sum of rigid-body inertia and added inertia:

$$\boldsymbol{I} = \begin{bmatrix} I_x & -I_{xy} & -I_{xz} \\ -I_{yx} & I_y & -I_{yz} \\ -I_{zx} & -I_{zy} & I_z \end{bmatrix}. \quad (5)$$

Owing to the symmetric design of GT-MAB, namely CM of the robot is on Z_B axis, the inertia matrix can be simplified as diagonal with $I_x = I_y$. Similarly, the term $\boldsymbol{\Omega} \times (\boldsymbol{I}\boldsymbol{\Omega})$ in Equation (4) can be neglected [14]. Therefore, the rotational motion of the GT-MAB can be simplified as:

$$\boldsymbol{I}\dot{\boldsymbol{\Omega}} = \boldsymbol{M} + \boldsymbol{\tau}. \quad (6)$$

Thus, the swing-related pitch and roll motion of GT-MAB can be decoupled as:

$$\begin{aligned} I_x\dot{p} &= M_x + \tau_x \\ I_y\dot{q} &= M_y + \tau_y \end{aligned}. \quad (7)$$

2.3.   Dynamic Model of Pitching Motion

As discussed in Section 2.2, pitch and roll dynamics of GT-MAB are decoupled and almost identical. Therefore we only focus on the pitch motion in dynamic modeling and identification. Hence, the attitude and angular velocity are assumed to be $\boldsymbol{\eta_2} = [0, \theta, 0]^\top$ and $\boldsymbol{\Omega} = [0, q, 0]^\top = [0, \dot{\theta}, 0]^\top$. For simplicity, we assume CM is the pivot of the pitching oscillation. Therefore the translational velocity at CM is zero when GT-MAB is hovering. Owing to the consistent CM position, we neglect the added mass effect for the translational motion. Thus we assume the total mass of GT-MAB, m, equals to the rigid-body mass of the blimp.
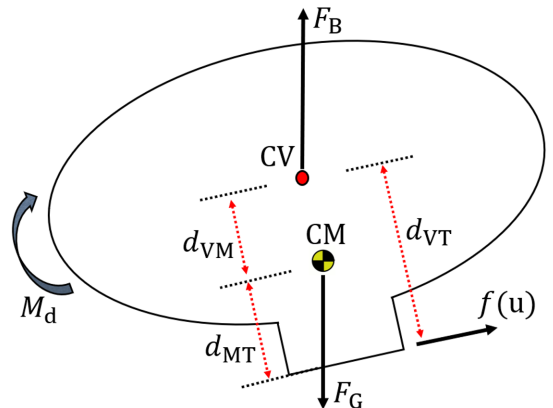

Fig. 3.   Side view of GT-MAB. Forces and moments that contribute to the pitching oscillation are annotated on the plot.

Fig. 3 demonstrates the major forces and moments while GT-MAB is pitching. The pair of forces, F_B and F_G, are the buoyancy and gravitational force at CV and CM. The distance between CV and CM is denoted as d_{VM}. Due to this bottom-heavy design, there is gravitational restoring torque, M_G, which stabilizes the blimp while it is pitching. $f(u)$ represents the motor thrust in X_B direction, where u is the controller output for the corresponding thruster. Since the thrusters are installed beneath the envelop, the motor-induced torque about CM, τ, will be generated. The rotational inertia and air damping moment about CM are denoted as I_{CM} and M_d separately. Therefore, the pitching motion of GT-MAB can be described as:

$$I_{CM}\dot{q} = I_{CM}\ddot{\theta} = M_d + M_G + \tau. \qquad (8)$$

The aerodynamic damping term, M_d, can be assumed to be linear to angular velocity $\dot{\theta}$ for low-speed indoor blimps [21]. Denote b as the damping coefficient, and M_d can be found as:

$$M_d = -bq = -b\dot{\theta}. \qquad (9)$$

The gravitational restoring torque, M_G, stabilizes the blimp given that the CM is below the center of buoyancy. This stabilization moment, M_G, can be represented as:

$$M_G = -F_B d_{VM} \sin(\theta). \qquad (10)$$

Due to the displacement between the thrusters and the pitching pivot, the thruster-induced torque τ is inevitable when motors are turned on. The torque τ can be found as:

$$\tau = d_{MT} f(u). \qquad (11)$$

Therefore, the pitching dynamics of GT-MAB described in Equation 8 can be expanded as:

$$I_{CM}\ddot{\theta} = -b\dot{\theta} - F_B d_{VM} \sin(\theta) + d_{MT} f(u). \qquad (12)$$

As illustrated in Fig. 3, the term d_{MT} can be written as $d_{MT} = d_{VT} - d_{VM}$, where d_{VT} is a constant parameter from the dimension measurements in Section 3.1. GT-MAB is neutrally ballasted prior to each flight, thus we can assume that the total buoyancy F_B is equal to the total gravitational force, hence $F_B = F_G = mg$, where g is gravitational constant. Therefore, the pitching dynamics in Equation (12) can be written as:

$$I_{CM}\ddot{\theta} = -b\dot{\theta} - d_{VM}\sin(\theta)mg - (d_{VT} - d_{VM})f(u). \qquad (13)$$

2.4.   Grey Box Model

The terms d_{VM}, d_{VT}, m, and $f(u)$ in Equation (13) can be calculated or measured with relatively good accuracy. However, the air damping coefficient b, and the moment of inertia I_{CM}, cannot be easily estimated due to the complex aerodynamics effects and the unconventional shape of GT-MAB. Therefore, a grey box model is constructed to represent the pitching dynamics of GT-MAB, where the model structure is explicitly specified, and the parameters are partially known. Denote the angle and angular rate of

GT-MAB's pitching motion as $\boldsymbol{x} = [\theta, \dot{\theta}]^\top$, and the grey box model can be represented as:

$$\begin{aligned}
\dot{x}_1 &= x_2 \\
\dot{x}_2 &= [-bx_2 - mgd_{VM}\sin(x_1) + (d_{VT} - d_{VM})f(u)]/I_{CM}.
\end{aligned} \qquad (14)$$

3.   Parameter Identification

This section discusses the parameter identification of the grey box model that describes the pitching dynamics of GT-MAB. The model with identified parameters is then linearized for controller design and validated with experimental data.

3.1.   The parameter d_{VT}

d_{VT} is the distance between the CV and the motor thrust force f, as demonstrated in Fig. 3. In contrast to large outdoor airships which usually adjust their buoyancy by changing the volume of air and helium, GT-MAB uses thrusters to adjust its altitude to reduce the size and improve maneuverability. Therefore, the dimension of GT-MAB is consistent, and can be considered as a rigid body when inflated. Owing to this, d_{VT} is a constant parameter and can be calculated as:

$$d_{VT} = H_{ENV}/2 + H_{GON}, \qquad (15)$$

where H_{ENV} and H_{GON} are the thickness of the envelop and the height of the gondola, as illustrated in Fig. 4. With the measurement $H_{ENV} = 0.44$m and $H_{GON} = 0.04$m, we have $d_{VT} = 0.26$m.
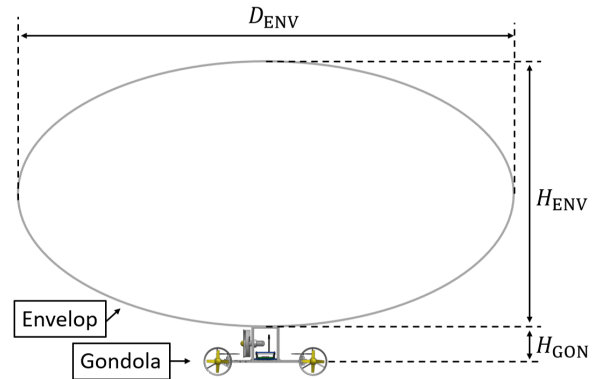

Fig. 4.   Dimension of the envelop and the gondola of GT-MAB.

3.2.   The thrust $f(u)$

$f(u)$ represents the mapping between the motor thrust and the input command. The command $u \in [-1, 1]$ represents the duty circle that controls the DC motor of GT-MAB.

Positive u will result in the motor thrusting in X_B direction, while a negative value will generate force oppositely. Neglecting the resistance of the electronics such as H-bridge, we can approximate the voltage applied on the motor as:

$$V_{\text{motor}} = V_{\text{batt}} \cdot u, \tag{16}$$

where V_{batt} is the voltage of the battery, which can be measured by the circuitry on GT-MAB. Similar to the work [21], we measure the motor thrust with a high-accuracy scale. The relationship between the motor thrust and the applied voltage can be seen in Fig. 5.
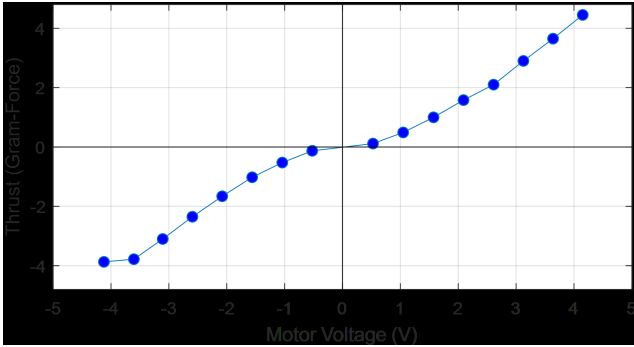

Fig. 5.   Motor thrust in X_B direction, versus the voltage applied on the motors, V_{motor}.

3.3.   *The total mass m*

The total mass of GT-MAB, m, is hard to be directly measured since the Helium gas inside the envelop cannot be easily gauged. Instead, by measuring the lifting force provided by the envelop, we can derive the total buoyancy of GT-MAB, and therefore find the total mass of the vehicle. Let F_{lift} be the lifting force provided by the envelop, which is equal to the total buoyancy F_{B} minus the gravitational forces of the Helium gas and the deflated envelop. Moreover, since GT-MAB is neutrally buoyant, F_{lift} equals to the gravitational force of all the components that are attached on the envelop, thus the gondola assembly, the ballast weight, and the localization trackers. Therefore, F_{B} and F_{lift} can be represented as follows:

$$\begin{aligned} F_{\text{lift}} &= F_{\text{B}} - (m_{\text{env}} + m_{\text{He}})g \\ &= (m_{\text{gon}} + m_{\text{mkr}} + m_{\text{blst}})g \end{aligned} \tag{17}$$

$$\begin{aligned} F_{\text{B}} &= (m_{\text{env}} + m_{\text{He}})g \\ &+ (m_{\text{gon}} + m_{\text{mkr}} + m_{\text{blst}})g, \end{aligned} \tag{18}$$

where m_{env}, m_{He}, m_{gon}, m_{mkr}, m_{blst} are the mass of the deflated envelop, helium gas, gondola assembly, localization makers, and the ballast weight to keep GT-MAB neutrally buoyant.

According to Archimedes' principle, and assuming the envelop dominates the volume of GT-MAB, we can find that the total buoyancy F_{B} is equal to the weight of air that the envelop displaces. Then, Eq. (18) for F_{B} can be written as:

$$\begin{aligned} F_{\text{B}} &= \rho_{\text{air}} V_{\text{env}} g \\ &= (m_{\text{env}} + m_{\text{He}})g \\ &+ (m_{\text{gon}} + m_{\text{mkr}} + m_{\text{blst}})g, \end{aligned} \tag{19}$$

where ρ_{air} and V_{env} are the density of air and the volume of the envelop. Given that the mass of the helium gas is:

$$m_{\text{He}} = \rho_{\text{He}} V_{\text{He}} = \rho_{\text{He}} V_{\text{env}}, \tag{20}$$

the volume of the envelop can be calculated as:

$$V_{\text{env}} = \frac{m_{\text{gon}} + m_{\text{mkr}} + m_{\text{blst}} + m_{\text{env}}}{\rho_{\text{air}} - \rho_{\text{He}}}. \tag{21}$$

Assuming the temperature of the indoor environment is around 300K (26.85°C), density of both helium and air is known as $\rho_{\text{He}} = 0.164\text{kg/m}^3$ and $\rho_{\text{air}} = 1.161\text{kg/m}^3$. With the total mass of the four components in Eq. (21) measured as 107.24 grams, the overall mass of GT-MAB, m, can be calculated as:

$$m = \rho_{\text{air}} V_{\text{env}} = 0.1249\text{kg}. \tag{22}$$

3.4.   *d_{VM} and initial approximation of I_{CM}*

With the mass of all components of GT-MAB measured and calculated in previous sections, we use CAD software to calculate the position of the CM, namely d_{VM}, and the rough estimation of the moment of inertia, I_{CM}. The estimated I_{CM} will be used as the initial approximation for the system identification experiments in Section 3.5.

As illustrated in Fig. 6, the envelop of GT-MAB is modeled as an ellipsoid in the CAD software. From work [35], dimension of the inflated envelop can be calculated by its deflated radius as:

$$\begin{aligned} r_{\text{in}} &\approx 0.7627 r_{\text{de}} \\ \tau_{\text{in}} &\approx 0.9139 r_{\text{de}} \end{aligned} \tag{23}$$

where r_{de} is the radius of the deflated envelop, and r_{in} and τ_{in} are the radius and thickness of the envelop when inflated. Therefore, the ellipsoid CAD model with dimension r_{in} and τ_{in} is constructed with measurement $r_{\text{de}} = 0.457\text{m}$. With Autodesk Inventor software [36], we found that $d_{\text{VM}} = 0.0971\text{m}$ and $I_{\text{CM}} = 0.00371\text{kg} \cdot \text{m}^2$.
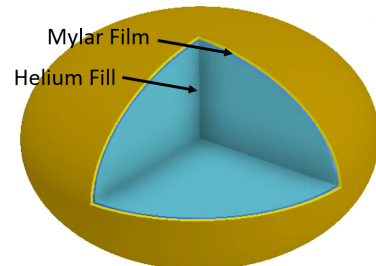

Fig. 6.   CAD model of the helium-filled envelop.

3.5. I_{CM} and b

Now I_{CM} and b are the only two unknown parameters in the grey box model described in Eq. (14). A series of system identification experiments are designed to obtain these parameters. GT-MAB is released with initial pitch angle θ_0, and the motion capture system (OptiTrack) logs the free response of the pitching oscillation. The experiment is repeated eight times with different initial angle θ_0. The first seven datasets are used for identifying the parameters and the last one is for validation.

As listed in Table 1, seven I_{CM} and b pairs are identified from the first seven datasets with MATLAB System Identification Toolbox [37]. Fig. 7 demonstrates both the logged pitch angle and the simulated response with the identified parameters from the first dataset. The fitting between the measured and modeled system is quantified as normalized root-mean-square error (NRMSE). The final estimations of I_{CM} and b are found as the average of the seven identified results in Table 1, which are $I_{CM} = 0.005821$kg $\cdot$ m^2 and $b = 0.000980$N $\cdot$ m $\cdot$ s/rad.

Table 1.   Parameters Identified from the Experimental Datasets

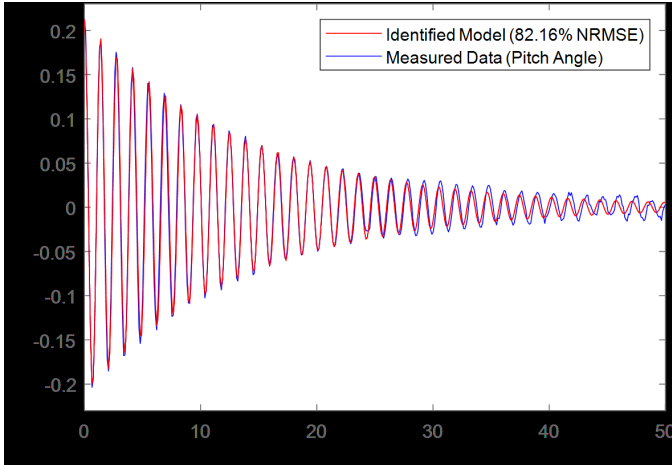| Dataset	I_{CM}	b	NRMSE Fit
Dataset 1	0.005782	0.000838	82.16%
Dataset 2	0.005847	0.000978	85.45%
Dataset 3	0.005835	0.000940	84.29%
Dataset 4	0.005828	0.001140	85.20%
Dataset 5	0.005851	0.001083	87.26%
Dataset 6	0.005750	0.001025	77.80%
Dataset 7	0.005855	0.000857	85.21%
Mean	0.005821	0.000980	83.91%

Fig. 7.   Measured pitching oscillation and the simulated response with the identify parameters from dataset 1.

3.6.   *Model Linearization and Validation*

Table 2 summarizes the parameters of the dynamic model obtained from the previous sections. Therefore, the pitching dynamic model of GT-MAB in Eq. (13) can be represented as:

$$\ddot{\theta} = -20.4284\sin(\theta) - 0.1684\dot{\theta} + 27.9933f(u). \qquad (24)$$

Table 2.   Parameters of GT-MAB's Pitching Dynamic Model

Parameters	Value
g	9.81 m/s^2
I_{CM}	0.005821 kg $\cdot$ m^2
b	0.000980 N $\cdot$ m $\cdot$ s/rad
m_{ASM}	0.1249 kg
d_{VT}	0.26 m
d_{VM}	0.097051 m

The identified model is then linearized around $\theta = \dot{\theta} = 0$ for controller design. The state-space representation of the linearized model can be written as:

$$\begin{bmatrix} \dot{\theta} \\ \ddot{\theta} \end{bmatrix} = \begin{bmatrix} 0 & 1 \\ -20.4284 & -0.1684 \end{bmatrix} \begin{bmatrix} \theta \\ \dot{\theta} \end{bmatrix} + \begin{bmatrix} 0 \\ 27.9933 \end{bmatrix} f(u). \quad (25)$$

This linearized model is compared with the eighth dataset discussed in Section 3.5 for validation. The linearized model has a satisfying 88.37% NRMSE fit with the validation data, which can be seen in Fig. 8.
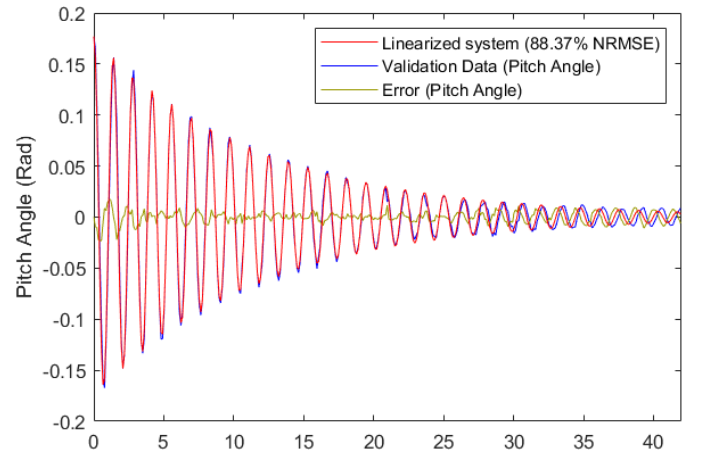

Fig. 8.   Measured pitching oscillation from the validation dataset and the simulated response with the linearized dynamic model.

8   *Q. Tao et al.*

4.   Flight Control System

As discussed in Section 1, the underactuated design, fluctuated position measurement, and control system latency are the major difficulties in stabilizing the swing oscillation of GT-MAB. In this section, a swing-reducing flight control system is developed to address these difficulties. Feedback controllers are designed to reduce the swing oscillation of this underactuated robot, the CM position is estimated and incorporated in controller design for less fluctuated position measurement, and control system latency is reduced by improving both hardware and software implementation of the platform.

4.1.   *System overview*

Fig. 9 demonstrates the overall setup of the flight control system. Pose of GT-MAB is estimated by tracking the localization markers on top of the envelop. A ground station computer interfaces the motion capture system, and runs the flight control software. The control commands are transmitted to GT-MAB via wireless communication, and the onboard electronics of the blimp drive the thrusters once a command is received.
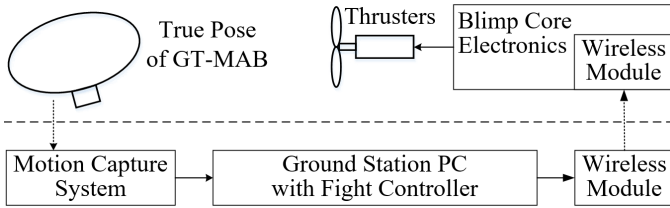
Fig. 9.   Overview of GT-MAB's flight control system.

4.2.   *System latency reduction*

The fast dynamics of the swing motion requires low latency from the flight control system. We reduce the latency by implementing the flight controller software with lower-level programming language, minimizing the response time of GT-MAB's onboard electronics and firmware, and enhancing the wireless communication. Owing to the efforts on reducing the latency, the update rate of the flight controller is raised to 120Hz. As shown in Fig. 10, an experiment is designed to measure the delay in the control loop. We use a rotational plate with markers to emulate the attitude of GT-MAB during swing oscillation. By comparing the rotation angle from the rotary encoder, and the voltage applied on the thruster, we found the latency of the control system is around 30.5ms. Compared to the period of the pitching oscillation from Fig. 7, which is approximately 1.3s, the control system latency can be neglected.
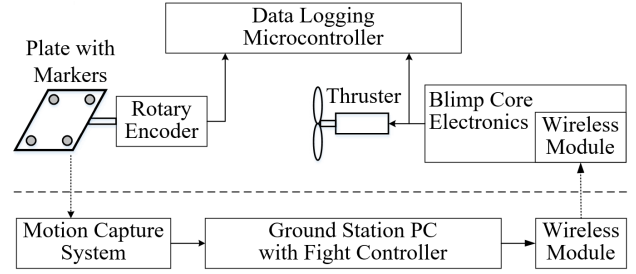
Fig. 10.   Experimental setup for measuring the latency of the control system.

To further reduce the response time of GT-MAB, coreless DC motors are chosen for its low rotor inertia. To evaluate the response time of the thrusters, we establish a second-order model that is simplified from work [38].

$$\begin{bmatrix} \dot{x}_1 \\ \dot{x}_2 \end{bmatrix} = \begin{bmatrix} 0 & 1 \\ 0 & -1/\tau \end{bmatrix} \begin{bmatrix} x_1 \\ x_2 \end{bmatrix} + \begin{bmatrix} 0 \\ \beta/\tau \end{bmatrix} V_{\text{motor}}, \qquad (26)$$

where x_1, x_2 represent the shaft angle and angular velocity of the thruster. The terminal voltage on the motor is denoted as V_{motor}. τ and β are time constant and static gain that characterize the motor response. With the experiment setup shown in Fig. 11, the step response of the thruster is collected. We fit the DC motor model to the measured response, and obtain the time constant $\tau = 28$ms. Compared to the period of the pitching oscillation, which is around 1.3s, the motor response time can be neglected.
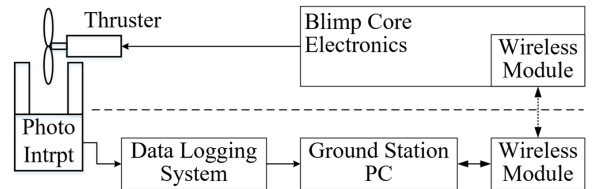
Fig. 11.   Experimental setup for measuring the thruster response of GT-MAB. A photo interrupter measures the angular velocity of the thruster without touching the motor shaft.

4.3.   *Center of Mass Position Estimation*

As shown in Fig. 12, the localization markers are placed at the top of GT-MAB for better visibility to the motion tracking cameras. However, due to the displacement between O_M and CM, the position measurement of the markers has large fluctuation while GT-MAB is swinging.
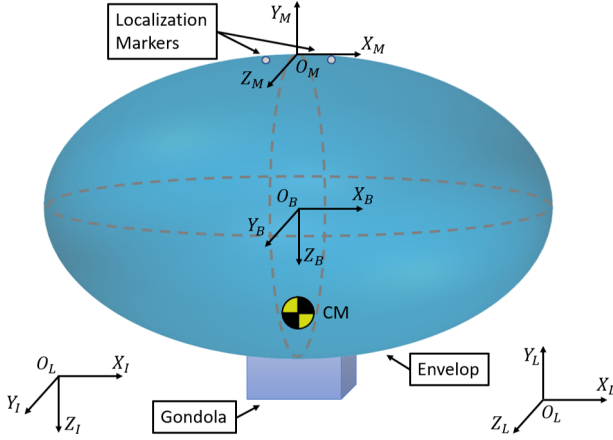
Fig. 12.   Offset between the localization makers O_M, and the CM of GT-MAB.

With identified parameters from Section 3, position of CM can be estimated from the pose measurement of the localization markers. We define the vector $^B\boldsymbol{p}_{\mathrm{CM}}$ to represent the position of CM in blimp's body frame. Given the fact that O_M is usually on Z_B axis, $^B\boldsymbol{p}_{\mathrm{CM}}$ can be simplified as:

$$^B\boldsymbol{p}_{\mathrm{CM}} = [0, 0, -d_{\mathrm{VM}}]^\top, \tag{27}$$

where d_{VM} is the distance between CV and CM identified in Section 3.1.

Since the only measurement from the motion tracking system is the pose of $O_M X_M Y_M Z_M$ in $O_L X_L Y_L Z_L$, a series coordinate transformations are required to find the CM position in the inertial frame. We begin with representing the vector $^B\boldsymbol{p}_{\mathrm{CM}}$ in $O_M X_M Y_M Z_M$:

$$^M\boldsymbol{p}_{\mathrm{CM}} = {}^M_B\boldsymbol{R}\,^B\boldsymbol{p}_{\mathrm{CM}} + {}^M_B\boldsymbol{q}, \tag{28}$$

where $^M_B\boldsymbol{R}$ is the rotation matrix between $O_B X_B Y_B Z_B$ and $O_M X_M Y_M Z_M$, and $^M_B\boldsymbol{q}$ is the position of O_B in $O_M X_M Y_M Z_M$. Since the relationship between these two frames are already known, we have:

$$^M_B\boldsymbol{R} = \begin{bmatrix} 1 & 0 & 0 \\ 0 & 0 & -1 \\ 0 & 1 & 0 \end{bmatrix} \tag{29}$$

$$^M_B\boldsymbol{q} = [0, -H_{\mathrm{ENV}}/2, 0]^\top.$$

Similarly, $^M\boldsymbol{p}_{\mathrm{CM}}$ can be represented in $O_L X_L Y_L Z_L$ as:

$$^L\boldsymbol{p}_{\mathrm{CM}} = {}^L_M\boldsymbol{R}\,^M\boldsymbol{p}_{\mathrm{CM}} + {}^L_M\boldsymbol{q}, \tag{30}$$

where $^L_M\boldsymbol{R}$ and $^L_M\boldsymbol{q}$ can be found as the attitude and position of the markers in the motion capture system. Then, the CM position in the inertial frame can be calculated as:

$$^I\boldsymbol{p}_{\mathrm{CM}} = {}^I_L\boldsymbol{R}\,^L\boldsymbol{p}_{\mathrm{CM}} + {}^I_L\boldsymbol{q}. \tag{31}$$

With the relation between $O_L X_L Y_L Z_L$ and $O_I X_I Y_I Z_I$ defined in Section 2.1, we know that:

$$^I_L\boldsymbol{R} = \begin{bmatrix} 1 & 0 & 0 \\ 0 & 0 & 1 \\ 0 & -1 & 0 \end{bmatrix} \tag{32}$$

$$^I_L\boldsymbol{q} = [0, 0, 0]^\top.$$

Therefore, with the simplified notation $c\cdot = \cos(\cdot)$ and $s\cdot = \sin(\cdot)$, the CM position in inertia frame can be found as:

$$^I\boldsymbol{p}_{\mathrm{CM}} = \begin{bmatrix} x_L + (\frac{H_{\mathrm{ENV}}}{2} + d_{\mathrm{VM}})(c\phi_L s\psi_L - c\psi_L s\theta_L s\phi_L) \\ z_L - (\frac{H_{\mathrm{ENV}}}{2} + d_{\mathrm{VM}})c\theta_L s\phi_L \\ -y_L + (\frac{H_{\mathrm{ENV}}}{2} + d_{\mathrm{VM}})(c\phi_L c\psi_L + s\phi_L s\psi_L s\theta_L) \end{bmatrix}, \tag{33}$$

where $[x_L, y_L, z_L]^\top$ and $[\phi_L, \theta_L, \psi_L]^\top$ are the position and Euler angles of the markers from the localization system.

4.4.   Feedback controller design

Station keeping is one of the most common operating scenarios of GT-MAB. A flight controller is designed to keep GT-MAB at the desired position while simultaneously compensates the swing oscillation. As shown in Fig. 13, the proposed method consists of a station-keeping controller that tracks the position and heading of GT-MAB, and a swing-reducing controller which reduces the roll and pitch oscillation of the robot.
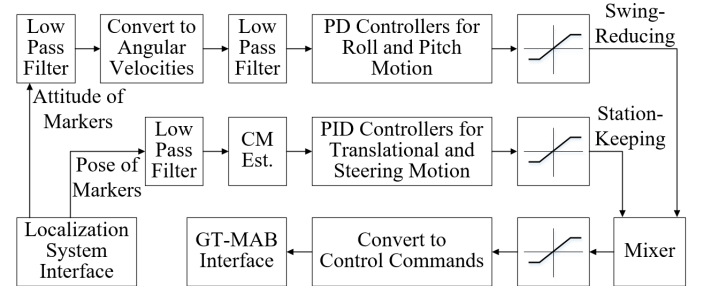

Fig. 13.   Functional block diagram of the controller design.

4.4.1.   Station-keeping controller

The station-keeping controller is an extension of our previous work [14]. The controller keeps the GT-MAB at the desired position $^I\boldsymbol{p}_{\mathrm{ref}} = [^I x_{\mathrm{ref}}, {}^I y_{\mathrm{ref}}, {}^I z_{\mathrm{ref}}]^\top$, and holds its heading at ψ_{ref}. As discussed in Section 4.3, the CM position of GT-MAB has significantly less fluctuation compared to that of the localization markers. Therefore, we use $^I\boldsymbol{p}_{\mathrm{CM}}$ to represent the position of GT-MAB. Hence, the distance and heading error can be calculated as:

$$^I\boldsymbol{e}_{\mathrm{pos}} = {}^I\boldsymbol{p}_{\mathrm{ref}} - {}^I\boldsymbol{p}_{\mathrm{CM}}$$
$$e_\psi = \psi_{\mathrm{ref}} - \psi. \tag{34}$$

Four PID controllers are implemented to minimize the position and the heading error. The controller outputs are denoted as u_x, u_y, u_z and u_ψ separately. Since the position errors are defined in the inertial frame, the controller outputs for the translational motion is then transferred to GT-MAB's body frame as:

$$[^B u_x, {^B}u_y, {^B}u_z]^\top = {^B_I}\boldsymbol{R}[u_x, u_y, u_z]^\top, \qquad (35)$$

where $^B_I R$ is the rotation matrix between the inertia and body frame.

4.4.2. Swing-reducing controller

The swing-reducing controller stabilizes the roll and pitch motion of GT-MAB during hovering flight. Given the roll and pitch dynamics of the blimp is decoupled and almost identical, we design the controller for the pitch motion, and then apply the same control law on the roll movement. From the linearized pitch model described in Eq. (25), there are two poles in the open-loop dynamics. Shown in Fig. 14, the two poles are located at $-0.0842 \pm 4.5190i$, indicating the open-loop dynamics is highly oscillatory with very limited damping. As a consequence, the undesired swing oscillation occurs once GT-MAB cannot damp the disturbance torque induced by the underactuated configuration. This issue becomes more significant when more powerful thrusters are installed for better maneuverability and flyability against airflow.

To reduce the oscillation of this stable but highly oscillatory system, a PD controller is designed to regulate the angular velocity of the pitch motion. As shown in Fig. 14, the closed-loop system under the PD controller has poles at -95.6275 and -0.0502, and zeros at 0 and -125. This indicates the closed-loop system has fast damping without oscillatory component.
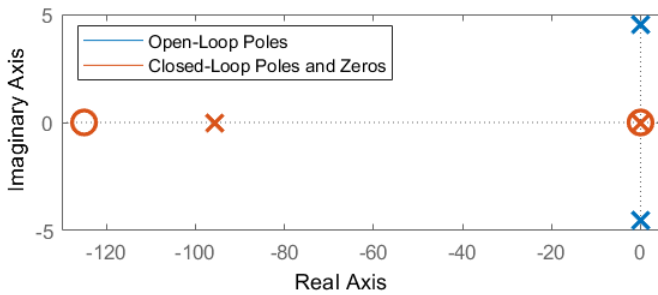

Fig. 14.   Pole and zero plot of both open-loop and closed-loop dynamics of GT-MAB's pitch motion.

The same PD controller is then being applied to control the angular velocities of both pitch and roll motion. Setpoints of both controllers are set to zero for stabilization purpose. The swing rate error can then be found as:

$$\boldsymbol{e}_{\mathbf{swing}} = [-p, -q]^\top, \qquad (36)$$

where p and q are the angular velocities of GT-MAB around X_B and Y_B axes in the body frame. From Eq. (3), these angular rates can be found as:

$$
\begin{aligned}
p &= \dot\phi - \dot\psi \sin\theta \\
q &= \dot\theta \cos\phi + \dot\psi \sin\phi \cos\theta,
\end{aligned}
\qquad (37)
$$

where ϕ, θ, and ψ are the roll, pitch, and yaw angles of GT-MAB. As illustrated in Fig. 14, low-pass filters are implemented to reduce the measurement noise from the localization system.

The outputs of the PD controllers are denoted as u_p and u_q for the roll and pitch motion separately. Since both p and q are defined in GT-MAB's body frame, the outputs can also be written as:

$$
\begin{aligned}
{^B}u_p &= u_p \\
{^B}u_q &= u_q.
\end{aligned}
\qquad (38)
$$

4.4.3. Mixer design

The outputs from both station-keeping and swing-reducing controllers are then mapped to the five gondola-mounted thrusters as shown in Fig. 15. The mixer is designed as:

$$
\begin{bmatrix} f_1 \\ f_2 \\ f_3 \\ f_4 \\ f_5 \end{bmatrix}
=
\begin{bmatrix}
1 & 0 & 0 & 0 & \frac{1}{2d_{\mathrm{MT1}}} & \frac{1}{d_{\mathrm{SM}}} \\
1 & 0 & 0 & 0 & \frac{1}{2d_{\mathrm{MT2}}} & \frac{-1}{d_{\mathrm{SM}}} \\
0 & 0 & 1 & 0 & 0 & 0 \\
0 & 0 & 1 & 0 & 0 & 0 \\
0 & 1 & 0 & \frac{-1}{d_{MT5}} & 0 & 0
\end{bmatrix}
\begin{bmatrix} {^B}u_x \\ {^B}u_y \\ {^B}u_z \\ {^B}u_p \\ {^B}u_q \\ {^B}u_\psi \end{bmatrix},
\qquad (39)
$$

where f_1 to f_5 are the propulsion force generated by the thrusters as denoted in Fig. 15. d_{MT1}, d_{MT2}, and d_{MT5} represents the distance between the CM and the thrusters with propulsion force f_1, f_2, and f_5 along Z_B axis. d_{SM} is the distance between the two surge motors with thrust force f_1 and f_2.
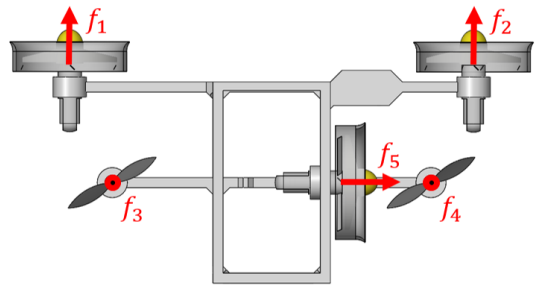

Fig. 15.   Top view of GT-MAB's gondola demonstrating the thruster configuration. Only the thrusters and the gondola frame are displayed for better illustration.

4.5. *Controller performance in experiments*

An experiment is designed to compare the proposed method to the traditional station-keeping controller without swing reduction feature.

We first fly the blimp only with the station-keeping controller by disabling the swing-reducing feature. Thus the control outputs $^B u_p$ and $^B u_q$ are both zero. The setpoints of the station-keeping controller are set to $^I \boldsymbol{p}_{\text{ref}} = [0, 0, 1.4]^\top$ and $\psi_{\text{ref}} = 0$ to keep GT-MAB hovering at the center of the indoor lab. As observed in Fig. 16, the GT-MAB starts swinging severely within 20 seconds. As discussed in Section 4.4.2, this swing oscillation is due to the damping in roll and pitch dynamics is insufficient to cancel the undesired torque from the underactuated configuration of GT-MAB.

With the same experimental setup, we repeat the test with the swing-reducing controller engaged. As can be seen in Fig. 17, the proposed flight control system is able to stabilize the swing motion of GT-MAB. Table 3 compared the variance of the roll and pitch angles before and after the swing-reducing controller is engaged. The variance is reduced by approximately two magnitudes once the swing-reducing controller is turned on.

Table 3. Variance of the roll and pitch angles of GT-MAB

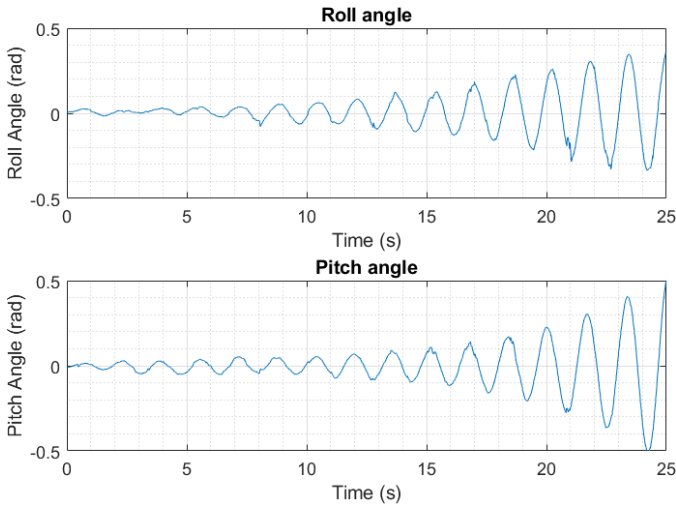| Parameters	Without Swing-Reduction	With Swing-Reduction
Variance roll	0.0133	8.1502e-05
Variance pitch	0.0174	2.5425e-04

Fig. 16. Roll and pitch angle of GT-MAB without swing-reducing controller.
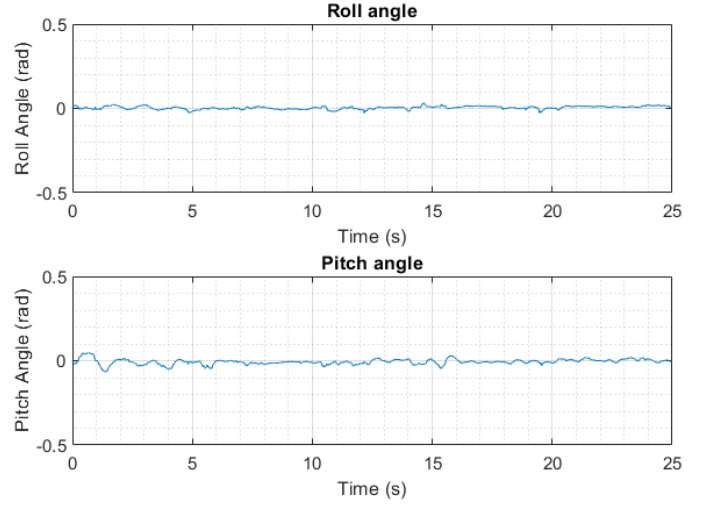

Fig. 17. Roll and pitch angle of GT-MAB with swing-reducing controller.

5. Conclusion and Future Work

This paper presents the modeling and control of the swing oscillation of GT-MAB, an underactuated indoor blimp. The dynamics of the swing motion is modeled, identified, and linearized for controller design. The linearized model with identified parameters shows a satisfactory fit with the validation data. A swing-reducing flight control system is designed for the station-keeping mission with features including reduced latency and CM position estimation. Flight test results demonstrate that the flight control system can stabilize the roll and pitch motion of GT-MAB, and effectively reduce the swing oscillation.

We plan to expand the dynamic model of GT-MAB by incorporating the coupling between the translational and rotational motions. The flight control system will also be upgraded to reduce the swing oscillation while GT-MAB is in translational movement.

Acknowledgments

12   Q. Tao et al.

References

[1] S. Grzonka, G. Grisetti, and W. Burgard. A fully autonomous indoor quadrotor. *IEEE Transactions on Robotics*, 28(1):90–100, Feb 2012.

[2] S. Bouabdallah, A. Noth, and R. Siegwart. Pid vs lq control techniques applied to an indoor micro quadrotor. In *2004 IEEE/RSJ International Conference on Intelligent Robots and Systems (IROS)*, volume 3, pages 2451–2456 vol.3, Sep. 2004.

[3] S. Shen, N. Michael, and V. Kumar. Autonomous multi-floor indoor navigation with a computationally constrained micro aerial vehicle. In *2011 IEEE International Conference on Robotics and Automation*, pages 2968–2969, May 2011.

[4] D. St-Onge, P.Y. Brches, I. Sharf, N. Reeves, I. Rekleitis, P. Abouzakhm, Y. Girdhar, A. Harmat, G. Dudek, and P. Gigure. Control, localization and human interaction with an autonomous lighter-than-air performer. *Robotics and Autonomous Systems*, 88:165 – 186, 2017.

[5] R. A. S. Fernndez, J. L. Sanchez-Lopez, C. Sampedro, H. Bavle, M. Molina, and P. Campoy. Natural user interfaces for human-drone multi-modal interaction. In *2016 International Conference on Unmanned Aircraft Systems (ICUAS)*, pages 1013–1022, June 2016.

[6] N. Yao, E. Anaya, Q. Tao, S. Cho, H. Zheng, and F. Zhang. Monocular vision-based human following on miniature robotic blimp. In *IEEE International Conference on Robotics and Automation (ICRA)*, 2017.

[7] B. Siciliano and O. Khatib. *Springer handbook of robotics*. Springer, 2008.

[8] Y. Bestaoui-Sebbane. *Lighter than air robots*. Springer Netherlands, 2012.

[9] A. Elfes, S. Siqueira Bueno, M. Bergerman, and J. G. Ramos. A semi-autonomous robotic airship for environmental monitoring missions. In *Proceedings. 1998 IEEE International Conference on Robotics and Automation*, volume 4, pages 3449–3455 vol.4, May 1998.

[10] T. Takaya, H. Kawamura, Y. Minagawa, M. Yamamoto, and A. Ohuchi. Pid landing orbit motion controller for an indoor blimp robot. *Artificial Life and Robotics*, 10(2):177–184, Nov 2006.

[11] F. Zhang, Q. Tao, T.J. Tan, P.S.T Cheng, S. Cho, V. Mishra, and J.P. Varnell. Miniature autonomous robotic blimp.

[12] N. Yao, Q. Tao, W. Liu, Z. Liu, Y. Tian, P. Wang, T. Li, and F. Zhang. Autonomous flying blimp interaction with human in an indoor space. *Frontiers of Information Technology & Electronic Engineering*, 20(1):45–59, Jan 2019.

[13] Q. Tao, M. King-Smith, A. Muni, V. Mishra, S. Cho, P. Varnell, and F. Zhang. Control theory - autonomous blimp. In *IEEE CSS Video Clip Contest*, 2015.

[14] S. Cho, V. Mishra, Q. Tao, P. Varnell, M. King-Smith, A. Muni, W. Smallwood, and F. Zhang. Autopilot design for a class of miniature autonomous blimps. In *Proc. of IEEE Conference on Control Technology and Applications (CCTA)*, 2017.

[15] Ning-shi Yao, Qiu-yang Tao, Wei-yu Liu, Zhen Liu, Ye Tian, Pei-yu Wang, Timothy Li, and Fumin Zhang. Autonomous flying blimp interaction with human in an indoor space. *Frontiers of Information Technology & Electronic Engineering*, 20(1):45–59, Jan 2019.

[16] A. G. Kendall, N. N. Salvapantula, and K. A. Stol. On-board object tracking control of a quadcopter with monocular vision. In *2014 International Conference on Unmanned Aircraft Systems (ICUAS)*, pages 404–411, May 2014.

[17] Yuwen Li, Meyer Nahon, and Inna Sharf. Airship dynamics modeling: A literature review. *Progress in Aerospace Sciences*, 47(3):217 – 239, 2011.

[18] Z. Ashraf and M. A. Choudhry. Dynamic modeling of the airship using analytical aerodynamic model. In *2009 International Conference on Emerging Technologies*, pages 188–193, Oct 2009.

[19] S. Kale, P. Joshi, and R. Pant. A generic methodology for determination of drag coefficient of an aerostat envelope using cfd. *AIAA 5th ATIO and 16th Lighter-Than-Air Sys Tech. and Balloon Systems Conferences*, 2005.

[20] S. B. V. Gomes and J. G. Ramos. Airship dynamic modeling for autonomous operation. In *Proceedings of IEEE International Conference on Robotics and Automation*, 1998.

[21] J. Shan. Dynamic modeling and vision-based control for indoor airship. In *International Conference on Mechatronics and Automation*, 2009.

[22] J.-C. Zufferey, A. Guanella, A. Beyeler, and D. Floreano. Flying over the reality gap: From simulated to real indoor airships. *Autonomous Robots*, 21(3):243–254, Nov 2006.

[23] F. Hayato and S. Akira. Wind-disturbance-based control approach for blimp robots. *Electronics and Communications in Japan*, 97(2):52–59.

[24] C. Wan, N. Kingry, and R. Dai. Design and autonomous control of a solar-power blimp. In *2018 AIAA Guidance, Navigation, and Control Conference, AIAA SciTech Forum*, 2018.

[25] Y. Wang, G. Zheng, D. Efimov, and W. Perruquetti. Altitude control for an indoor blimp robot. *IFAC-PapersOnLine*, 50(1):15990 – 15995, 2017. 20th IFAC World Congress.

[26] Q. Tao, J. Cha, M. Hou, and F. Zhang. Parameter identification of blimp dynamics through swinging motion. In *2018 15th International Conference on Control, Automation, Robotics and Vision (ICARCV)*, pages 1186–1191, Nov 2018.

[27] V. Srisamosorn1, N. Kuwahara, A. Yamashita1, T. Ogata, and J. Ota. Design of face tracking system using fixed 360-degree cameras and flying blimp for health care evaluation. In *The 4th International Conference on Serviceology*, 2016.

[28] D. Palossi. Self-sustainability in nano unmanned aerial vehicles: A blimp case study. In *CF'17 Proceedings of the Computing Frontiers Conference*, 2017.

[29] P. Gonzalez, W. Burgard, R. Sanz, and J. L. Fernandez. Developing a low-cost autonomous indoor blimp. *Journal of Physical Agents*, 2009.

[30] S. Bermudez i Badia, P. Pyk, and P. F. M. J. Verschure. A biologically based flight control system for a blimp-based uav. In *Proceedings of the 2005 IEEE International Conference on Robotics and Automation*, pages 3053–3059, April 2005.

[31] T. Takaya, H. Kawamura, Y. Minagawa, M. Yamamoto, and A. Ouchi. Motion control in three dimensional round system of blimp robot. In *2006 SICE-ICASE International Joint Conference*, pages 1291–1294, Oct 2006.

[32] H. Kawamura, M. Yamamoto, T. Takaya, and A. Ohuchi. Learning landing control of an indoor blimp robot for self-energy recharging. *Artificial Life and Robotics*, 12(1):116–121, Mar 2008.

[33] H. Kawamura, H. Iizuka, T. Takaya, and A. Ohuchi. Cooperative control of multiple neural networks for an indoor blimp robot. *Artificial Life and Robotics*, 13(2):504–507, Mar 2009.

[34] M. Mahn and M. Kemper. A behaviour-based navigation system for an autonomous indoor blimp. *IFAC Proceedings Volumes*, 39(16):837 – 842, 2006. 4th IFAC Symposium on Mechatronic Systems.

[35] I. M. Mladenov. On the geometry of the mylar balloon. *Comptes Rendus de l'Academie Bulgare des*, 2001.

[36] About mass properties. Autodesk Knowledge Network, [Accessed: 28- Jun- 2018].

[37] L. Ljung. *System Identification Toolbox User's Guide*. MathWorks, Inc, 3 Apple Hill Drive Natick, MA 01760-2098, March 2018.

[38] L. Ljung. *System identification: Theory for the User*. Prentice Hall PTR, 2 edition, 1999.